JACS
JOURNAL OF THE AMERICAN CHEMICAL SOCIETY
pubs.acs.org/JACS
Article

Recognition of Surface Oxygen Intermediates on NiFe Oxyhydroxide Oxygen-Evolving Catalysts by Homogeneous Oxidation Reactivity

Yaming Hao, Yefei Li,* Jianxiang Wu, Lingshen Meng, Jinling Wang, Chenglin Jia, Tao Liu, Xuejing Yang,* Zhi-Pan Liu, and Ming Gong*

Cite This: J. Am. Chem. Soc. 2021, 143, 1493−1502

Read Online

ACCESS | Metrics & More | Article Recommendations | Supporting Information

ABSTRACT: NiFe oxyhydroxide is one of the most promising oxygen evolution reaction (OER) catalysts for renewable hydrogen production, and deciphering the identity and reactivity of the oxygen intermediates on its surface is a key challenge but is critical to the catalyst design for improving the energy efficiency. Here, we screened and utilized in situ reactive probes that can selectively target specific oxygen intermediates with high rates to investigate the OER intermediates and pathway on NiFe oxyhydroxide. Most importantly, the oxygen atom transfer (OAT) probes (e.g., 4-(diphenylphosphino) benzoic acid) could efficiently inhibit the OER kinetics by scavenging the OER intermediates, exhibiting lower OER currents, larger Tafel slopes, and larger kinetic isotope effect (KIE) values, while probes with other reactivities demonstrated much smaller effects. Combining the OAT reactivity with electrochemical kinetic and operando Raman spectroscopic techniques, we identified a resting Fe═O intermediate in the Ni−O scaffold and a rate-limiting O−O chemical coupling step between a Fe═O moiety and a vicinal bridging O. DFT calculation further revealed a longer Fe═O bond formed on the surface and a large kinetic energy barrier of the O−O chemical coupling step, corroborating the experimental results. These results point to a new direction of liberating lattice O and expediting O−O coupling for optimizing NiFe-based OER electrocatalyst.

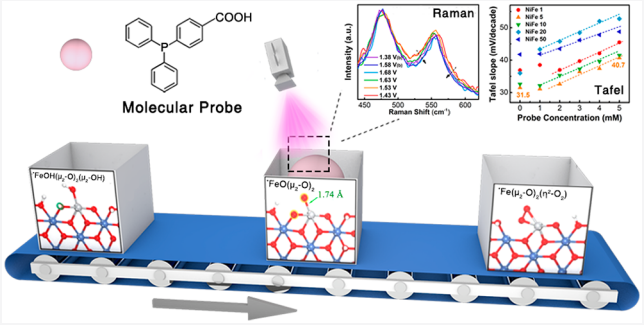

INTRODUCTION

The oxygen evolution reaction (OER) has played a pivotal role in the pursuit of hydrogen economy as a sustainable energy solution.[1−4] Its sluggish kinetics involving the transfer of four electrons and protons accounts for most of the energy penalty required for water electrolysis, and therefore the development of highly efficient and low-cost OER electrocatalysts is desired.[3,5−10] In light of this, NiFe oxyhydroxide, often derived from in situ electrochemical oxidation of NiFe layered double hydroxide (NiFe LDH), represents one of the most active electrocatalysts for alkaline OER and has attracted tremendous attention over the past years.[11−14] The incorporation of Fe in the octahedral Ni site drastically increases the OER activity as well as reduces the Tafel slope. Its facile and scalable synthesis also makes it affordable and promising for large-scale alkaline water electrolyzers.

Recent efforts have been dedicated to understanding the molecular-level OER mechanism on NiFe oxyhydroxide surfaces to further facilitate the design and optimization of the catalyst.[14−25] A variety of electrochemical and in situ spectroscopic techniques have been utilized for the mechanistic studies. For instances, structural analyses with X-ray absorption spectroscopy (XAS) revealed the formation of Fe^{4+} isolated sites in NiOOH as the active site with the aid of DFT calculation,[16] which was further evidenced by in situ Mossbauer spectroscopy.[17] Scanning electrochemical microscopy (SECM) study further identified two types of sites with one fast kinetics site correlating well with the Fe content in the catalyst film, demonstrating the essential role of Fe in OER.[19] In addition to Fe, another in situ XAS study observed higher Ni oxidation state of +3.6 in NiFe oxyhydroxide, and attributed the OER activity to the charge transfer between Ni and Fe through Ni−O−Fe.[26] Despite that the active site is still in debate, these studies have provided important clues about the metal identities of NiFe oxyhydroxide during OER catalysis. Alternatively, the surface oxygen intermediates associated with the metal sites play indispensable roles in the redox transitions toward dioxygen generation. According to the calculation studies, the optimal binding of oxygen intermediates on the NiFe oxyhydroxide surface is critical to lowering the OER energy barrier.[27−30] Specifically, Carter et al. proposed an

Received: October 27, 2020
Published: January 13, 2021

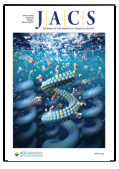

https://dx.doi.org/10.1021/jacs.0c11307
J. Am. Chem. Soc. 2021, 143, 1493−1502

optimized OER pathway with molecule-like oxygen intermediates that can fulfill the catalytic cycle at low overpotentials on Fe-doped β-NiOOH surfaces,[27] but experimental evidence is currently still lacking due to the low averaged signals of the transient oxygen intermediates. Some limited spectroscopic analyses by Raman spectroscopy and ambient pressure X-ray photoelectron spectroscopy (AP-XPS) have achieved little success in identifying the oxygen intermediates formed on NiFe oxyhydroxide.[15,22,25] Therefore, developing new tools for probing oxygen intermediates under operating conditions is still highly desired for understanding the OER mechanism.

Herein, we took inspiration from the use of molecular probes in catalytic studies,[31,32] and systematically designed and screened reactive probes that can interfere with the OER kinetics to investigate the oxygen intermediate reactivity and the OER mechanism on NiFe oxyhydroxide surfaces. We adopted typical homogeneous oxidation reactivity of oxygen atom transfer (OAT) and hydrogen atom transfer (HAT) for the design of our probes. The probes with OAT reactivity were discovered to competitively inhibit the OER process, while probes with other reactivities exhibited smaller effects. Detailed comparison with and without probe conditions in combination with competitive kinetics, isotope exchange experiments, and operando Raman spectroscopy allowed us to successfully identify the key resting intermediates and the rate-determining step (rds) of OER on NiFe oxyhydroxide catalysts. According to the experimental evidence, we proposed a molecular-level OER pathway on NiFe oxyhydroxide surfaces, which was further supported by DFT calculation.

RESULTS AND DISCUSSION

Designing and Screening of Reactive Probes. The general principle for the proposed reactive probe method utilizes the competition between the reactions of the electrochemically generated surface oxygen intermediates with reactive probes and the OER counterparts to generate dioxygen. The introduction of reactive probes can theoretically scavenge specific oxygen intermediates and alter the electrochemical reaction pathway. Since the two pathways with and without reactive probes can drastically differ in kinetics parameters, rds, and key intermediates, we can glean the chemical properties of the oxygen intermediates as well as the molecular-level OER pathway in a comparative manner with the aid of kinetic and spectroscopic techniques (Scheme 1).

The selection of reactive probes is critical to this study. First, the probe should contain a reactive center that can react with surface oxygen intermediates at high rates and high specificity. The high rates ensure the efficient trapping of oxygen intermediates to compete with the OER kinetics, and the high specificity facilitates the identification of oxygen intermediates via its reactivity. We took inspiration from the well-studied reactivities in homogeneous catalytic oxidation and utilized typical reactivities of oxygen atom transfer (OAT) and hydrogen atom transfer (HAT). OAT probes, often including phosphines, thioethers, and alkenes, can specifically target oxygen-terminated structures for abstracting oxygen atoms.[33−35] HAT probes, often C−H-based molecules, can specifically target oxygen-associated high-valent metal species, such as metal oxo and metal peroxo species, for donating H atoms to generate the corresponding radical.[36,37] These reactivities can widely exist on the oxygen intermediates formed during OER and we anticipate that probes with different reactivity can behave divergently, allowing for the differentiation and identification of oxygen intermediates. To be compatible with in situ experiments, the reactive probes should also demonstrate high solubility and chemical stability in the electrolyte. In addition, the probes should not contain multiple reactive centers or high degrees of freedom that may complicate the reactivity on catalyst surfaces. Accordingly, we incorporated the solubility handles of carboxylate owing to its high solubility under alkaline conditions, and the solubility handle was separated from the reactive center by a rigid aromatic scaffold (Scheme 1).

Scheme 1. (a) Illustration of the Probe Method for the OER Mechanistic Study;[a] (b) Design Principle of the Molecular Probes and the Representative Probes Used in the Current Study

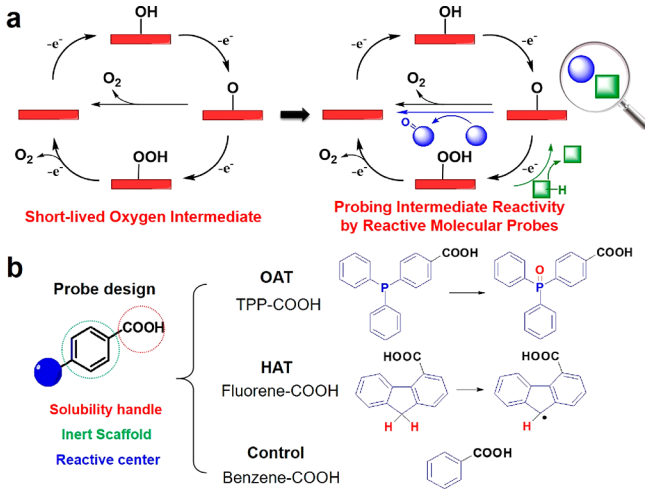

[a]The high-rate reactivity of the probe with the oxygen intermediates can tackle the challenging problem of transient intermediates that restricts current mechanistic study.

On the basis of the probe design principle, we selected a series of reactive probes that are either commercially available or easily accessible by a simple single-step reaction, and screened their chemical and electrochemical stability in alkaline electrolytes. For instance, the thioanisole-based probe that is typically used for investigating OAT reactions[38] exhibited considerable degradation by nucleophilic OH^- attack in alkaline electrolytes, and therefore was excluded for this study (Figures S1−S3 of the Supporting Information, SI). After screening, we selected 6 representative reactive probes (2 OAT, 2 HAT, and 2 control probes) (Figures S4−S15), among which we used 4-(diphenylphosphino) benzoic acid (TPP−COOH), fluorene-4-carboxylic acid (Fluorene−COOH), and benzoic acid (Benzene−COOH) as the OAT, HAT, and control probe more extensively throughout this study.

Competitive Kinetics Study under Probe Titration. The NiFe LDH precatalyst electrodes for this study were prepared by a facile electrodeposition method. The as-derived electrode exhibited uniformly distributed nanoflower-like particles of NiFe LDH on the carbon fibers (Figures S16 and S17). The pristine catalyst showed a Ni oxidation state of +2 and a Fe oxidation of +3 that are consistent with NiFe LDH according to XPS (Figure S18). A typical CV curve involves a pair of $Ni^{2+}/Ni^{\delta+}$ ($\delta \geq 3$) redox peaks to form the oxyhydroxide phase at 1.30−1.50 V vs RHE,[39] followed by the OER onset at ∼1.45 V vs RHE (Figure 1a). Interestingly,

https://dx.doi.org/10.1021/jacs.0c11307
J. Am. Chem. Soc. 2021, 143, 1493−1502

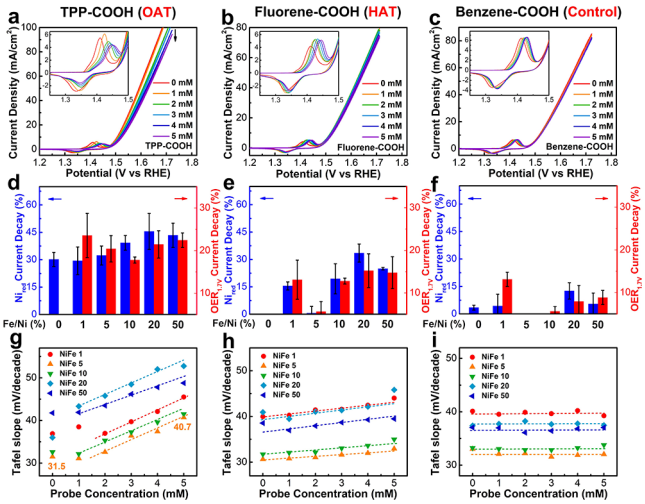

Figure 1. (a–c) Cyclic voltammetry curves of the NiFe 5 (Fe/Ni = 5%) catalysts in 1 M KOH with the titration of 0–5 mM probes, (a) TPP–COOH, (b) Fluorene–COOH, and (c) Benzene–COOH. The scan rate is 5 mV/s. The insets show the Ni redox features upon the probe titration. (d–f) The change in the two parameters of $Ni^{\delta+}$ reduction current and OER current at 1.7 V vs RHE over different NiFe LDH catalysts with varied Fe/Ni ratios under the addition of 5 mM (d) TPP–COOH, (e) Fluorene–COOH, and (f) Benzene–COOH in the electrolyte. The parameters are derived from the cyclic voltammetry curves, which are listed in Figures S4–S15. Multiple repetitive measurements using different batches of catalysts were carried out to calculate the mean values and standard deviations to confirm the probe effects. (g–i) The calculated Tafel slopes over different NiFe LDH catalysts with varied Fe/Ni ratios under different probe concentrations of (g) TPP–COOH, (h) Fluorene–COOH, and (i) Benzene–COOH. The resistances are reported in the SI.

the titration of TPP–COOH (OAT probe) gradually lowered the OER current in a concentration-dependent manner, accompanied by the positive shift of Ni^{2+} oxidation as well as the decreased current of $Ni^{\delta+}$ reduction during the reverse scan (Figure 1a). Under 5 mM TPP–COOH, all NiFe oxyhydroxide catalysts with different Fe/Ni ratios consistently exhibited ~20% OER current decay and ~30–50% $Ni^{\delta+}$ reduction current decay (Figure 1d). These probe effects were currently restrained by the limited solubility (~10 mM for TPP–COOH), but could be more pronounced under stirring conditions to break the mass transport limitations. An additional OER current decay of ~11.2% and a $Ni^{\delta+}$ reduction current decay of ~19.2% could be observed at a stirring speed of 500 rpm (Figure S19). To eliminate the possibility that TPP–COOH serves as a poison to the catalyst, we carried out potentiostatic measurements with intermittent probe addition and clearly resolved instantaneous current decays upon each TPP–COOH addition (Figure S20). The current continued to decay for a certain period after the instantaneous decrease, which we attributed to the possible interaction with the carboxylate group that demands some structural reorientation for a maximal probe effect. Importantly, the OER activity could be almost completely recovered when reverting back to no probe conditions, excluding the irreversible poisoning effect (Figure S20).

In contrast to TPP–COOH, significantly smaller changes of the OER current and $Ni^{\delta+}$ reduction current were observed upon the titration of the HAT probe (Fluorene–COOH) and the control probe (Benzene–COOH) (Figure 1b,c). The HAT probe could lead to ~10–15% OER current decay and ~15–30% $Ni^{\delta+}$ reduction current decay, while the control probe could only lead to <10% OER current decay and <15% $Ni^{\delta+}$ reduction current decay (Figure 1e,f). The general trend of OAT > HAT > control was confirmed by utilizing other probes with similar reactivities (Figures S4–S15). The extra OER current decay of the NiFe 1 catalyst in all cases was attributed to its slightly lower stability, resulting in partial current decay over the kinetics measurement (Figure S21). Since the OAT probes specifically target oxygen-terminated surfaces, the larger OAT probe effect indicates that the key OER intermediates could be oxygen-terminated species. Notably, neither OAT or HAT probes could affect the OER kinetics of the Ni oxyhydroxide catalyst without any Fe (Figure 1d–f), suggesting that the key intermediates on Ni oxyhydroxide greatly differ from those on NiFe oxyhydroxide and follow a distinct OER pathway.[40] It also supports that the oxygen intermediates on Fe sites are the main probe target sites. By combining with the aforementioned oxygen-terminated resting state, we hypothesize that the key OER intermediates involve the molecular-like Fe=O moiety that is often subject to OAT reactivity.[34,35]

Tafel analysis is a useful electrochemical tool to investigate the rds and reaction pathway during electrocatalysis. Our NiFe oxyhydroxide catalysts all exhibited typical Tafel slopes of 30–40 mV/decade, among which the NiFe 5 catalyst (Fe/Ni = 5%) demonstrated the lowest Tafel slope of 31.5 mV/decade, close to a theoretical value of 30 mV/decade (Figure 1g). According to the Tafel equation and its parameter calculations (eqs 1–3),[6,41] where η is the OER overpotential, b is the Tafel slope, α is the transfer coefficient, η_b is the number of electrons transferred before rds, υ is the number of rds in the overall reaction, n_r is the number of electrons participating in the rds, and β is the symmetry factor that is often around 0.5.

$$\eta = a + b\log i \quad \text{(Tafel equation)} \tag{1}$$

$$b = \frac{\partial\eta}{\partial\log i} = \frac{2.303RT}{\alpha F} \tag{2}$$

$$\alpha = \frac{n_b}{\upsilon} + n_r\beta \tag{3}$$

A Tafel slope of 30 mV/decade implies a possible rate-limiting chemical step and two electron transfers before this chemical step with $n_b = 2$, $\upsilon = 1$, and $n_r = 0$.[42] Upon the titration of TPP–COOH, the Tafel slope showed a stepwise increase from ~30 to ~40 mV/decade (Figure 1g). The high-rate reaction between the resting oxygen intermediates and TPP–COOH causes the initial rds to be no longer rate-limiting and shifts the rds toward prior steps with the second highest energy barrier. In accordance, a Tafel slope of 40 mV/decade corresponds to the rds of the second electron-transfer or PCET (with $n_b = 1$, $\upsilon = 1$, and $n_r = 1$), which could be one step prior to the original rds with 30 mV/decade.

In previous reports, two possible rds with high energy barriers were proposed: one is the oxidation step of Fe–OH to Fe=O, and the other is the O–O coupling step.[27−30] On the basis of our experiments, the rate-limiting oxidation of Fe–OH to Fe=O is very unlikely due to the reasons that (1) transferring two electrons before this rds can hardly be achieved, (2) the resting state of Fe–OH cannot be kinetically affected by OAT probes, and (3) the rds of Fe–OH oxidation is not a chemical step that is inconsistent with a Tafel slope of

https://dx.doi.org/10.1021/jacs.0c11307
J. Am. Chem. Soc. 2021, 143, 1493−1502

30 mV/decade. The rate-limiting O−O coupling step is a better match.[29] The Fe═O resting state has strong OAT reactivity and can be efficiently scavenged by the OAT probe to alter the kinetics. Meanwhile, the catalytic cycle upon probe addition shifts the O−O coupling rds to the former Fe−OH oxidation step that is highly consistent with the Tafel study. Contrary to the OAT probes, the Benzene−COOH control probe demonstrated negligible changes to Tafel slopes under varied doses (Figure 1i), while the Fluorene−COOH HAT probe could reproducibly elevate the Tafel slope by a minor extent of 2−3 mV/decade (Figure 1h). This effect could be expected due to the typical HAT reactivity of the proposed Fe═O intermediate that is often found in heme or nonheme catalysts.[36] Since the HAT reactivity highly depends on the C−H bond strength, the subtle differences disappeared when using 4-methylbenzoic acid (Toluene−COOH) as the probe, suggesting the incapability of benzylic C−H oxidation by the oxygen intermediates on NiFe oxyhydroxide catalysts (Figures S10 and S11). Despite that Fluorene−COOH has one of the weakest C−H bonds, it still possesses tremendously lower effects than TPP−COOH, which indicates that the electrochemically generated Fe═O intermediates on hydroxide/oxyhydroxide surfaces have a larger tendency to donate the O atom with OAT reactivity than abstract an H atom with HAT reactivity. This reactivity greatly differs from the Fe-based homogeneous catalysts, and further points to the uniqueness of the hydroxide/oxyhydroxide scaffold for OER catalysis.

One of the unique advantages of using reactive probes is the high versatility of combining with other techniques for the comprehensive understanding of the elemental reaction steps. We further incorporated the probe strategy into the kinetic isotope H/D exchange experiments by comparing 1 M KOD in D_2O and 1 M KOH in H_2O electrolytes side by side to investigate the participation of H in the rds (Figures 2a,b and S22).[32] Without any probes, the catalyst exhibited parallel Tafel curves but with slightly inferior OER current in KOD to that in KOH. The k_H/k_D value was further calculated to be in the range of 1.37−1.40, representing a secondary kinetic isotope effect (KIE) that does not involve direct H-related bond breaking process in the rds (Figure 2b). In addition to the OER current decrease and Tafel slope increase, increasing doses of TPP−COOH displayed a steady increase of k_H/k_D values, reaching 1.64−1.67 at 7.5 mM TPP−COOH (Figure 2b). The increasing KIE values suggest the shift of a secondary KIE toward a primary KIE that involves direct H-related bond breaking event as the limiting step. The altered pathway was further evidenced by the lower apparent activation energy upon OAT probe addition (Figure S23). Such altered pathway under TPP−COOH could effectively transfer the rds to the elemental step with second largest energy barriers, leading to an overall apparent activation energy. These results agree well with our proposal of the rate-determining O−O coupling step with no direct H participation and the rate-limiting O−H bond breaking during Fe−OH oxidation into Fe═O after probe addition.

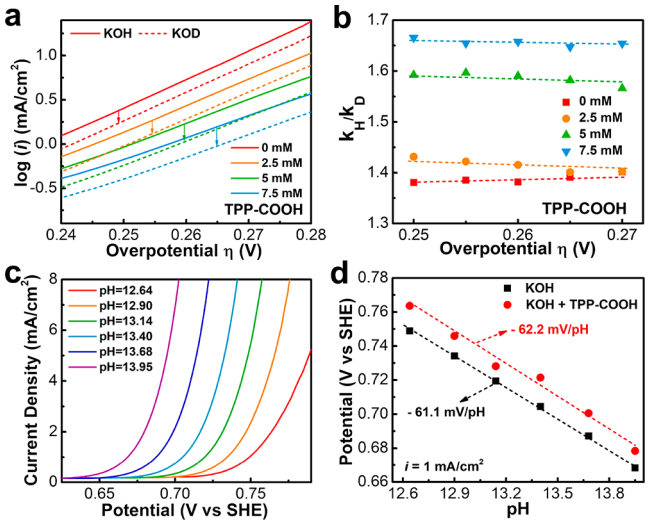

Figure 2. (a,b) The Tafel plots of NiFe 5 catalysts in 1 M KOH with varied concentrations of TPP−COOH under H/D exchange (1 M KOH in H_2O and 1 M KOD in D_2O). The scan rate is 0.5 mV/s. (b) The calculated k_H/k_D values under varied concentrations of TPP−COOH over different overpotentials. (c) The typical cyclic voltammetry curves of NiFe 5 catalysts under different pHs (R = 1.8 Ω). (d) The potentials at current densities of 1 mA/cm^2 on NiFe 5 catalysts in 1 M KOH and 1 M KOH + 5 mM TPP−COOH under different pHs. The slope corresponds to the Nernst shift.

In spite of the identification of the resting Fe═O intermediates, the molecular aspects of the rate-limiting O−O coupling step are less understood. When analyzing the $Ni^{\delta+}$ reduction and OER current decays at 1.7 V upon probe addition, we obtained an interesting Pearson correlation coefficient of 0.867 (Figure S24). The Pearson coefficients were smaller at low overpotentials than high overpotentials (Figure S24), likely because the carboxylate probes could partially occupy the surfaces to slightly lower the currents that contributes to a small amount of current decay and is relatively irrelevant to the Ni redox. The large Pearson coefficient at OER-relevant conditions indicate that there is a strong correlation between the OER current and the Ni redox. Since the structural Fe sites mainly accounted for the probe target as indicated earlier, such correlation involving Ni redox might represent the strong electronic communication between Ni and Fe sites, or in other words, the Ni sites may participate in the rate-limiting O−O coupling step, although the key oxygen intermediates are located on Fe sites. On the basis of the Fe═O intermediates and a rate-limiting chemical step, there might be two possible origins of the O−O coupling step: (1) the formation of surface-bound OOH by the transfer of one solution-phase OH^- onto Fe═O; 2) direct O−O coupling of Fe═O by the lattice O or OH. These two possibilities could give rise to different Nernst potential shifts per pH, since the involvement of additional OH^- in the rds could lead to a larger Nernst shift. Under different pHs in the 12.5−14.0 regime, we observed parallel Nernst shifts of the polarization curves (Figure 2c). By plotting the potentials at a current density of 1 mA/cm^2 over pHs (this current density was selected to minimize the influence of different Tafel slopes), we could derive the potential shifts of 61.1 and 62.2 mV/pH without and with the addition of TPP−COOH respectively, which are very close to the theoretical value of 59.1 mV/pH that corresponds to one H^+/OH^- per electron transfer (Figure 2c,d).[6] We attribute this pH shift to a rate-limiting lattice O-driven O−O coupling rather than the attack of solution-phase OH^- during the rds, because otherwise it should involve total of $3OH^-$ and $2e^-$ transfer corresponding to a larger potential shift of ∼90 mV/pH accordingly.[43] Under TPP−COOH, the shift of rds toward Fe−OH oxidation involves a total of $2OH^-$ and $2e^-$ transfers, consistent with the

https://dx.doi.org/10.1021/jacs.0c11307
J. Am. Chem. Soc. 2021, 143, 1493−1502

observed Nernst shift. Since the lattice O represents the bridging O between Fe and Ni, its participation in OER could explain the strong electronic communication between Ni and Fe sites in the catalyst.

Operando Raman Spectroscopy with OAT Probes. We further combined our reactive probe approach with spectroscopic techniques to facilitate the identification of surface oxygen intermediates. We first confirmed the OAT and HAT reactivities by the mass spectroscopy (MS) and nuclear magnetic resonance (NMR) analysis of the transformation products after the potentiostatic electrolysis (Figures S25 and S26). Complete conversion of TPP−COOH into TPPO−COOH under typical OAT reactivity was observed, while only partial oxidation of Fluorene−COOH was detected under identical conditions. It is in consensus with the observed trend in the probe effects. Owing to its compatibility with aqueous electrolyte system for operando measurements, Raman spectroscopy has been widely adopted to probe the reactive intermediates during catalytic OER processes. For examples, Bell et al. identified a surface bound OOH intermediate on gold electrodes by Raman spectroscopy.[44] Hu et al. combined the Raman spectroscopy with the active NiFe-based electrocatalysts to correlate the OER activity with structural disorders.[15] We envision that by using reactive probes such as TPP−COOH, an increase or decrease of the intermediate signal should be viable due to the efficient trapping of the oxygen intermediates. The Raman spectra showed characteristic peaks of $\delta(Ni^{III}-O)$ and $\upsilon(Ni^{III}-O)$ band at Raman shifts of 474 and 544 cm^{-1}, respectively, as well as the broad bands at around 800−1200 cm^{-1} previously attributed to the superoxide anion ($-OO^{-}$) intermediates, which are consistent with previous studies[14] (Figures 3b and S27).

Astonishingly, we observed highly resembling Raman patterns upon TPP−COOH addition except for the appearance of a peak at 1066 cm^{-1} (Figure 3b). By analyzing the liquid electrolyte containing TPP−COOH before and after Raman measurement, we observed the evolution of the 1066 cm^{-1} peak in addition to the aromatic peak at 1000 cm^{-1}, which was possibly attributed to the P═O bond generated in the oxidized probe (Figure 3a). Its successful detection by operando Raman spectroscopy not only confirmed the OAT reactivity but also supported the scavenging of oxygen-terminated species upon the addition of TPP−COOH. Although subtle changes were observed in addition to the P═O peak (Figure S28), the identical patterns at 800−1200 cm^{-1} might evidence that the broad peak of superoxide anion might not be related to OER, because TPP−COOH should hinder the OER pathway and bypass superoxide formation, theoretically leading to a significant decrease in the superoxide signal. This speculation correlates well with the presence of this band under non-OER conditions. We render that this band may belong to the bridging superoxide species or other surface oxygen species that is structurally relevant to Ni^{2+} oxidation but less relevant to OER.

In spite of the overall similarity of the Raman spectra, we focused our attention on the Ni−O peak region of 400−650 cm^{-1} and discovered subtle changes under different potentials with the addition of TPP−COOH. Specifically, when we normalized the Raman spectra based on the 474 cm^{-1} peak, we discovered that the 554 cm^{-1} peak was slightly narrower under TPP−COOH (Figure 3c,d). The peak width at 80% intensity was narrower by 4−6 cm^{-1} and the relative peak integration ratio of I_{554}/I_{474} was lower by 10−15% under OER conditions

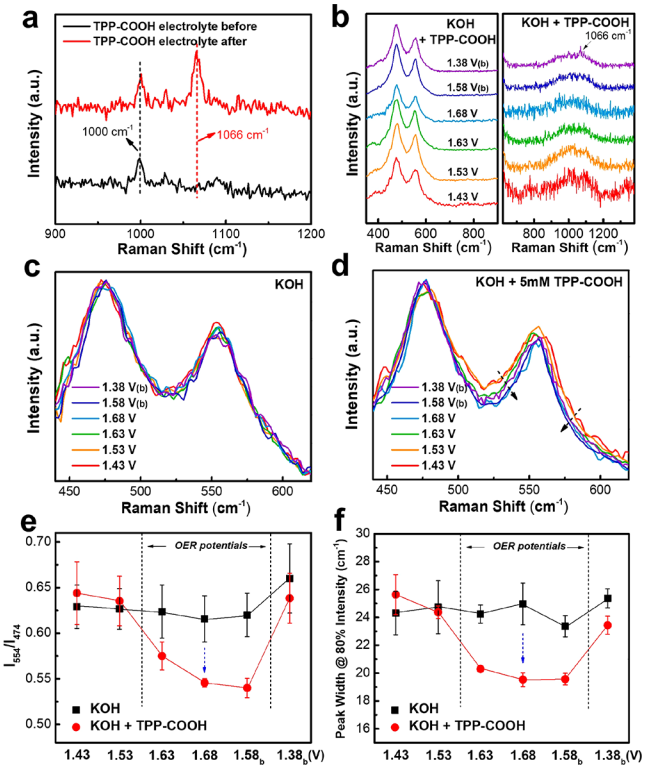

Figure 3. (a) The Raman spectra of the electrolyte (1 M KOH + 5 mM TPP−COOH) before and after electrolysis for the Raman study. (b) The Raman spectra of the NiFe 5 catalyst in 1 M KOH + 5 mM TPP−COOH under different applied potentials. 1.38 V (b) and 1.58 V (b) indicate the measurement on the reverse scans. (c,d) Comparison of the normalized Raman spectra of the NiFe 5 catalyst in (c) 1 M KOH and (d) 1 M KOH + 5 mM TPP−COOH under different applied potentials. (e,f) The calculated relative intensity ratio of I_{554}/I_{474} and the 554 cm^{-1} peak width at 80% peak intensity in 1 M KOH and 1 M KOH + 5 mM TPP−COOH under different applied potentials. Multiple repetitive measurements were carried out to calculate the mean values and standard deviations to confirm the probe effects.

compared to non-OER conditions (Figure 3e,f). Such differences were only observed with the presence of TPP−COOH, advocating the significance of using reactive probes for operando spectroscopic study. We calculated the theoretical Raman shifts of terminal Fe═O and bridging Fe−O−Ni species to be around 639, 531, and 586 cm^{-1} respectively (Figure S29), and therefore the narrower peak at 554 cm^{-1} was unlikely to be caused by the diminishing Fe═O intermediates, but instead was derived from bridging O species near the Fe centers. In previous reports, the relative ratio of I_{554}/I_{474} was reported to be a signature of the structural disorder in Ni oxyhydroxide, and the incorporation of Fe can induce the elevation of this value by increasing structural disorder, which correlates well with the OER activity.[22] According to our observations, we speculated that the efficient scavenge of Fe═O intermediates by OAT probes can reduce the Fe centers and decrease the local structural disorder by maintaining the structure at a relatively low oxidation state, which in turn decelerated the OER process. This decrease in local structural disorder possibly stemmed from the vanishing bridging O species in Fe−O−Ni and the decreased availability of bridging O species affects the OER kinetics due to its strong involvement in the rate-determining O−O coupling step as

https://dx.doi.org/10.1021/jacs.0c11307
J. Am. Chem. Soc. 2021, 143, 1493−1502

lattice O. To our knowledge, this could serve as the first spectroscopic evidence of the participation of bridging O species in Fe−O−Ni during the OER of NiFe oxyhydroxide catalyst. As Fe═O intermediates may have relatively fast turnover rates and low surface densities, and Raman studies of Fe═O intermediates in heme-based catalysts often require freeze−quench techniques, we could only observe obscure peaks for the differential Raman spectra in the Raman shift range of 600−700 cm^{-1} that might belong to the diminishing Fe═O intermediates under highly oxidative potentials (Figure S30). Therefore, further efforts on spectroscopically identifying Fe═O intermediates on the NiFe oxyhydroxide surfaces are still desired and ongoing.

OER Mechanism and Theoretical Calculation. On the basis of our kinetic and spectroscopic experiments, we carried out the systematic deduction of the molecular-level OER pathway (Figure 4a). The detailed correlation between the

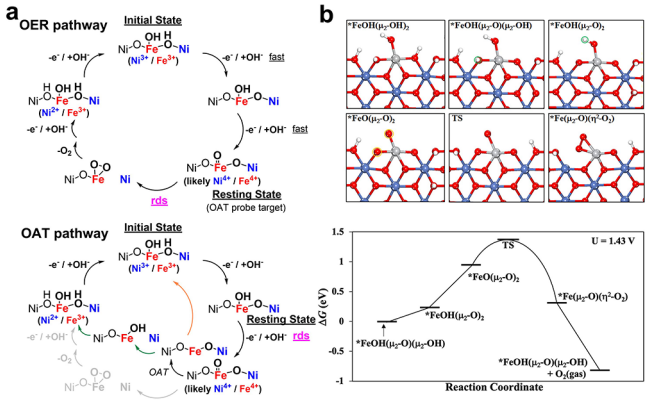

Figure 4. (a) The proposed mechanism of OER catalytic cycle with and without the OAT probe addition. (b) Structures for key intermediate states of OER and energetic profiles for OER on Fe-doped γ-NiOOH ($\bar{1}2\bar{1}0$) by PBE+U functions. Free energy changes are calculated at the electrode potential (U) at 1.43 V vs RHE. The small green cycles highlight the protons that are released in the subsequent step. The orange cycles highlight the O atoms that generate a surface peroxide. *FeOH(μ_2-OH)$_2$ is the surface state without applied potential, while *FeOH(μ_2-O)(μ_2-OH) is the initial state for OER. The nomenclature of coordination complexes (e.g., μ and η is utilized to represent the terminal structures of Fe ion; the asterisk * represents the Fe ion as a surface atom of γ-NiOOH; blue balls: Ni; gray balls: Fe; red balls: O; and white balls: H).

oxygen intermediate, Tafel slope, KIE, and OAT/HAT reactivity can be found in the SI. The initial state of the catalyst is critical to the mechanistic analysis, because the kinetic parameters can vary drastically according to the different initial states. Since OER is only observed after the completion of Ni^{2+} oxidation and Fe is mostly stable in its +3 oxidation state before the OER potential, we anticipate that the initial state involves Ni^{3+} and Fe^{3+} in the oxyhydroxide form, which can be viewed as the one-electron oxidized form of NiFe LDH with Ni^{2+} and Fe^{3+}. Without applied potential, the central site of NiFe LDH can be abbreviated as *FeOH(μ_2-OH)$_2$ with two μ_2-OHs connected to the Ni^{2+}; with applied OER potential, one-electron oxidation of Ni is accompanied by the release of one proton into the solution, generating *FeOH(μ_2-O)(μ_2-OH) with the μ_2-O connected to Ni^{3+}. This *FeOH(μ_2-O)(μ_2-OH) state is designated as the initial state for OER. Since the transfer of two electrons has to be completed before the rds according to the Tafel analysis, the initial state undergoes consecutive electron transfers from the initial state of Ni^{3+}/Fe^{3+} to form the resting state of *FeO(μ_2-O)$_2$ containing either Ni^{4+}/Fe^{4+} or Ni^{3+}/Fe^{5+}. The oxidative transition to Ni^{4+} is more likely according to previous observation of higher Ni oxidation state on NiFe oxyhydroxide surface.[26] We also calculated the on-site spin of the metal sites by DFT calculations and observed the decreased spin density on Ni sites upon oxidation, supporting the possible formation of Ni^{4+} species (Table S2). It is noteworthy that the Ni and Fe sites have strong electronic communication to relax any high-oxidation states for lowering the overall energy, and therefore the oxidation states of Ni and Fe could vary according to the local environment. In this *FeO(μ_2-O)$_2$ intermediate, Fe═O is mainly responsible for the greatly affected OER kinetics by the OAT reactivity. Following the resting intermediate, the rds is the subsequent step of breaking Ni−O bond and transfer of O to form a cyclic Fe peroxide intermediate with O−O coupling as its chemical nature, forming *Fe(μ_2-O)(η^2-O_2). This step is a chemical step, which is consistent with the Tafel slope and kinetic isotope experiments, but from kinetic aspects, it could be rather unfavored by involving one Ni−O bond breaking and one O−O bond formation in a single transition. As a consequence, it might involve large chemical energy barriers to be rate-limiting to the entire pathway. The use of lattice O or μ_2-O for dioxygen formation is evidenced by the Nernst shift and Raman spectroscopy study. Following the rds, the as-derived cyclic peroxide intermediate can further release the oxygen and eventually be subject to a series of OH^- and electron transfers to regenerate the surface. Under the addition of TPP−COOH, the resting state of *FeO(μ_2-O)$_2$ is rapidly scavenged by OAT reactivity to form *Fe(μ_2-O)$_2$, which can be subject to a series of reactions to regenerate the initial state but bypass the OER pathway.

In order to further validate our proposal, we carried out the DFT calculations by PBE+U functions (see SI for the calculation details). We used a deprotonated β-NiOOH structure by removing 2/3 protons to model the structure of γ-NiOOH and specifically used the γ-NiOOH ($\bar{1}2\bar{1}0$) surface as the model surface (Figure S31). Our previous study on γ-NiOOH has shown that the calculations based on this simplified model can yield an overpotential comparable with the experimental data.[45] We used a potential of U = 1.43 V vs RHE to represent the onset of OER processes. On the basis of the initial state of FeOH(μ_2-O)(μ_2-OH), the first PCET step facilely releases a proton from the surface upon oxidation (*FeOH(μ_2-O)(μ_2-OH) → *FeOH(μ_2-O)$_2$ + H^+ + e^-) with a Gibbs free energy change of +0.23 eV (Figure 4b). After that, the terminal *Fe−OH can undergo a second PCET to form *Fe═O, (*FeOH(μ_2-O)$_2$ → *FeO(μ_2-O)$_2$ + H^+ + e^-), and this step has a relatively higher Gibbs free energy change of 0.71 eV. Despite the fact that the following step of (*FeO(μ_2-O)$_2$ → *Fe(μ_2-O)(η^2-O_2)) is exothermal by 1.03 eV, this chemical step has a relatively high energy barrier of 0.41 eV (Figure 4b). It is worth mentioning that the nature of the chemical step determines that its energy barrier is significantly less influenced by the potentials than other electron-involved steps. Consequently, this energy barrier of the chemical step can be a rate-determining factor for the OER process, which is highly consistent with the experimental results. We also evaluated the energetic profile of K^+ and H_2O intercalated Fe-doped γ-NiOOH as another model catalyst, where a crystal structure with a formula of $K_{0.33}NiO_2{\cdot}0.66H_2O$, as we proposed in previous literature,[46] was utilized. Even though

https://dx.doi.org/10.1021/jacs.0c11307
J. Am. Chem. Soc. 2021, 143, 1493−1502

the energy barrier was lowered by 0.3 eV, a relatively large energy barrier for the chemical O−O coupling step was still present, further supporting our mechanistic proposal (Figure S32). After the O−O coupling, an O_2 molecule desorbs from the η^2-O_2 site, and then water molecules heal the remaining lattice O vacancy to regenerate the initial state *FeOH(μ_2-O)(μ_2-OH). These steps are highly exothermic and require less energy input compared with the first three steps, so we skip the details of these processes.

We further checked the energetic profile using hybrid HSE06 with α = 0.15, the identical parameter used by Carter et al.[27] which demonstrates a good description for the free energy changes for OER on Ni oxyhydroxide. A similar energy profile with the identical rds and large kinetic energy barrier of the chemical O−O coupling step was obtained, further corroborating the proposed mechanism (Figure S33). The proposed mechanism resembles the pathway with molecule-like sites proposed by Carter et al.[27] and the Mars van Krevelen mechanism proposed by Dionigi, Zeng, Cuenya, and Strasser et al.[47] The major difference lies in the proposed rate-determining step, which they tentatively designate to the Fe−OH oxidation with high thermodynamic energy barriers while what we render belongs to the kinetically unfavored O−O coupling step due to the probe effect and high energy barrier of the chemical O−O coupling step.

Interestingly, the bond length of Fe═O is determined to be 1.74 Å, which is longer than that in conventional Fe-oxo compounds. Accompanied by the elongation of the Fe═O bond, we could derive some spin density on the O atom in the Fe═O moiety, implying the decreased Fe═O bond strength to approach the radical-like species (Table S2). This decreased Fe═O bond strength can favor the OAT reaction by donating the O atom to the substrate, advocating the strong influence of the OAT probe to the OER kinetics and implying the probably higher tendency of forming O−O bonds on this Fe═O site. Moreover, we also calculated the free energy change of the OAT reaction between the active *FeO(μ_2-O)$_2$ and the reactive TPP core (*FeO(μ_2-O)$_2$ + TPP → *FeO-TPP(μ_2-O)$_2$) to demonstrate the high rate OAT reactivity. It turns out that this reaction is strongly exothermic with a free energy change of −4.56 eV, suggesting almost spontaneous oxygen abstraction upon TPP-based probe addition. This high-rate reaction sets up the basis for the mechanistic study by the probe approach. This mechanism is enabled only by combining the kinetic and spectroscopic study with the reactive probe approach, demonstrating a practical way of investigating mechanistic pathways with high turnover rates and transient intermediates using probes.

CONCLUSIONS

In summary, we have screened and utilized reactive probes with homogeneous oxidation reactivity to investigate the chemo-reactivity of oxygen intermediates during OER on NiFe oxyhydroxide catalysts. The representative OAT probe of TPP−COOH can effectively react with oxygen intermediates and alter the OER kinetics by lowering the OER current by ∼20% and increasing the Tafel slope by up to 10 mV/decade. Comparatively, the HAT probes and control probes exhibited significantly lower effects. The strong influence on OER by OAT reactivity manifests the key intermediates of oxygen-terminated surfaces. Further combination of the negligible probe effect on Ni oxyhydroxide catalysts and the altered KIE values under TPP−COOH successfully identifies the resting Fe═O intermediate during OER. The calculated Fe═O bond length of ∼1.74 Å is much larger than conventional Fe═O bonds, corroborating the favored OAT reactivity. Moreover, incorporating the OAT probe into operando Raman spectroscopy reveals the declination of bridging O signals in Fe−O−Ni moieties, suggesting the possible participation of bridging O in the rds. Further evidence by Nernst shift and Tafel analysis under probe conditions point to the rds of O−O coupling between Fe═O and a nearby bridging O. According to these findings, we propose a molecular-level OER mechanism on NiFe oxyhydroxide and DFT calculation supports its feasibility by demonstrating a relatively high energy barrier of the chemical O−O coupling step. Expediting O−O coupling and liberating lattice O are, thus, highly critical for NiFe catalyst design to further increase the catalytic efficiency. This mechanism was only enabled by the combination of reactive probes and kinetic/spectroscopic techniques, which can be further generalized to other catalyst systems.

EXPERIMENTAL SECTION

Chemicals. All reagents were used as-received without further purification. Nickel nitrate hexahydrate ($Ni(NO_3)_2{\cdot}6H_2O$, 98%), iron nitrate nonahydrate ($Fe(NO_3)_3{\cdot}9H_2O$, AR), Cobalt nitrate hexahydrate ($Co(NO_3)_2{\cdot}6H_2O$, 99%), 4-diphenylphosphino-benzoic acid (TPP−COOH, >97%), 4-methylbenzoic acid (Toluene−COOH, 98%), 4-hydroxybenzoic acid (Phenol−COOH, 99%), 4-vinylbenzoic acid (Styrene−COOH, 97%), 4-(methylthio) benzoic acid (Thioanisole−COOH, > 97%), Deuterium oxide (98% atom% D, D_2O), and ethanol (≥99.7%) were purchased from Aladdin Industrial Corporation (China). Benzoic acid (Benzene−COOH, ≥ 99.5%) and potassium hydroxide (≥85 wt %, KOH) were obtained from Sinopharm Chemical Reagent Co., Ltd. (China). Potassium deuteroxide solution (40 wt % in D_2O, 98% atom% D, KOD) was purchased from Sigma-Aldrich. Fluorene-4-carboxylic acid (Fluorene−COOH, 98%) was purchased from TCI (Shanghai). Anion exchange membrane was purchased from Fumatech (FAB-PK-130, Germany). Carbon fiber paper was purchased from Hesen Electric Co., Ltd. (HCP020N, China). Ultrapure deionized water (18.2 MΩ·cm^{-1}, 25 °C) was obtained from ELGA purification system (China).

Catalyst Electrode Preparation. The NiFe layered double hydroxide (LDH) catalyst precursors with different stoichiometric ratios of Ni/Fe were prepared by an electrodeposition method. Specifically, the electrodeposition was conducted in an electrochemical cell with a two-electrode configuration. 0.1 M $Ni(NO_3)_2{\cdot}6H_2O$ and x mM (x = 0, 1, 5, 10, 20, 50) $Fe(NO_3)_3{\cdot}9H_2O$ aqueous solution was used as the electrolyte, and carbon fiber paper (CFP) with an active area of 1 × 1 cm^2 was used as both the working electrode and counter electrode. The electrodeposition was carried out under a constant cathodic current density of 5 mA·cm^{-2} for 60 s (except for a current density of 20 mA·cm^{-2} for NiFe 50 due to the highly acidic electrolyte at high Fe contents). After electrodeposition, the electrode was washed with ethanol and ultrapure deionized water, and further dried in a vacuum oven at 60 °C before its use for the electrochemical measurement. Due to the kinetic-driven electrodeposition process, the trend of Ni/Fe ratios in the catalyst was consistent with the Ni/Fe precursor ratios in the electrolyte, as indicated by energy dispersive spectroscopy (EDS). Slightly higher Fe contents were observed possibly due to the higher sensitivity of Fe species to pH changes.

Electrochemical Kinetics Studies. The electrochemical kinetics studies were performed on CHI 660E potentiostat (Shanghai Chenhua Instruments Co.) using a standard 100 mL H-type electrochemical cell with a three-electrode configuration. A graphite rod was used as the counter electrode; an Ag/AgCl electrode (immersed in saturated KCl) was used as the reference electrode; and the as-prepared NiFe LDH catalyst electrode was used as the working electrode. The electrolyte was 1 M KOH aqueous solution unless

https://dx.doi.org/10.1021/jacs.0c11307
J. Am. Chem. Soc. 2021, 143, 1493−1502

specified. Cyclic voltammetry (CV) curves and linear sweep voltammetry (LSV) curves under the scan rates of 5 mV/s and 0.5 mV/s, respectively, were used for the kinetics study. The CV and LSV curves were not *iR*-corrected and the detailed resistance values are listed in Table S1 and figure legends. For obtaining accurate Tafel slope values, all Tafel plots were *iR*-corrected. In a titration experiment, 5 mM reactive probes were added successively with each portion of 1 mM, and following each addition, we carried out voltammetry measurements. All experiments were conducted at thermostatic water bath under a constant temperature of 30 °C, except that the experiments for calculating the apparent activation energies were conducted at thermostatic water bath under different temperatures. All measured potentials were converted to the reversible hydrogen electrode (RHE) according to the equation of $E_{RHE} = E_{Ag/AgCl} + 0.197 + 0.0591 \times pH$. The H/D exchange experiment was carried out under almost identical conditions except that a 30 mL H-type electrochemical cell was used to minimize the use of KOD and D_2O. 1 M KOD in D_2O was prepared by diluting 40 wt % KOD in D_2O with D_2O, and the electrolyte with TPP−COOH addition was prepared before the measurement. The same electrode was used for both KOH and KOD experiments for reliable measurements, and the pH of the solution was calibrated by pH meter (PHSJ-3F, INESA Scientific Instrument Co. Ltd., China). The potential shifts under KOH/H_2O and KOD/D_2O conditions were also confirmed by the onset potential of Ni^{2+} oxidation peaks in addition to the pH correction.

Characterization. The electrodeposited NiFe LDH (NiFe 5) on carbon fiber paper was used as the sample. The field emission scanning electron microscopy (FESEM) images were recorded on the ZEISS MERLIN Compact. Transmission electron microscopy (TEM) images were obtained on a FEI Talos S-FEG. X-ray photoelectron spectroscopy (XPS) data were obtained on a Thermo Scientific K-Alpha using a Al Kα X-ray source ($h\nu$ = 1486.6 eV).

The Raman spectra were recorded by Raman spectrometer (Horiba Jobin Yvon) equipped with a 532 nm laser. The resolution is about 1.3 cm^{-1}. A 2400/mm grating was used; the acquisition time was set as 50 s; the spectral Raman shift range was set from 200 to 1800 cm^{-1}. The operando Raman spectroscopy was conducted on a custom-built three-electrode cell (EC-RAIR, Beijing Science Star technology Co., Ltd.), with the Pt wire as the counter electrode, the Ag/AgCl electrode as the reference electrode (immersed in saturated KCl) and a roughened gold surface as the working electrode.

The NiFe 5 catalyst for the operando Raman spectroscopic study was prepared by a modified electrodeposition method on the roughened gold electrode. The electrodeposition condition was almost identical except that a lower current of 1 mA·cm^{-2} and a longer deposition duration of 120 s were used. The working electrode was further dried in vacuum at 30 °C after washing with ultrapure deionized water and ethanol. Before the spectroscopic study, the electrodes were preactivated by CV scans in 1 M KOH electrolyte to stabilize the electrode at a scan rate of 40 mV/s. The Raman spectra were collected afterward by sweeping the electrode to the designated potential range. The 1 M KOH + 5 mM TPP−COOH electrolyte before and after electrolysis was sealed in a capillary tube with an inner diameter of 1 mm for Raman measurement.

Product Analysis. The product analysis of the probe transformation during the electrochemical measurement was performed after the constant potential electrolysis of the electrolyte containing 5 mM probes at 1.62 V vs RHE for 2 h. The electrolyte after the electrolysis was neutralized by dilute sulfuric acid to form white precipitate. The precipitate was further filtered and washed with ultrapure deionized water to remove the residual salt. Finally, the precipitate was dried in the vacuum oven at 60 °C, and redispersed in CH_3OH or $CDCl_3$ for characterization purposes. As for control, the MS or NMR spectra of pure TPP−COOH and Fluorene−COOH were collected by dispersing in CH_3OH or $CDCl_3$, respectively.

The product analysis was first conducted by the nano ESI−MS on the A LTQ XL Orbitrap hybrid instrument (Thermo Fisher Scientific). The product dissolved in CH_3OH was directly fed to the instrument. The MS inlet temperature was 275 °C and spray voltage of negative 1.5 kV was used. The distance between the tip of the spray emitter and ion transfer capillary to the MS was held constant at ca. 1 mm. The product dissolved in $CDCl_3$ was characterized by NMR spectroscopy on Avance III HD 400 MHz Bruker.

■ ASSOCIATED CONTENT

Supporting Information

The Supporting Information is available free of charge at https://pubs.acs.org/doi/10.1021/jacs.0c11307.

Calculation details, mechanistic analysis and supporting figures showing the kinetic OER behaviors of NiFe oxyhydroxide under the titration of different probes and different stirring speed, SEM images, TEM images and XPS spectra of the as-prepared catalysts, potentiostatic electrolysis behaviors under probe addition, original CV curves under kinetic isotope experiments, OER/Ni redox correlation figure, mass and NMR spectra of the electrolysis products, original operando Raman spectroscopy data, structures and Raman modes of the catalyst for calculation, calculated OER energetic profile using HSE06, and behavior of CoFe LDH under TPP−COOH probe (PDF)

■ AUTHOR INFORMATION

Corresponding Authors

Yefei Li − *Key Laboratory of Computational Physical Science, Fudan University, Shanghai 200438, P. R. China;* orcid.org/0000-0003-4433-7433; Email: yefeil@fudan.edu.cn

Xuejing Yang − *National Engineering Laboratory for Industrial Wastewater Treatment, East China University of Science and Technology, Shanghai 200237, P. R. China;* orcid.org/0000-0001-5144-4400; Email: xj.yang@ecust.edu.cn

Ming Gong − *Department of Chemistry and Shanghai Key Laboratory of Molecular Catalysis and Innovative Materials, Fudan University, Shanghai 200438, P. R. China;* orcid.org/0000-0002-1584-1211; Email: gongm@fudan.edu.cn

Authors

Yaming Hao − *Department of Chemistry and Shanghai Key Laboratory of Molecular Catalysis and Innovative Materials, Fudan University, Shanghai 200438, P. R. China*

Jianxiang Wu − *Department of Chemistry and Shanghai Key Laboratory of Molecular Catalysis and Innovative Materials, Fudan University, Shanghai 200438, P. R. China*

Lingshen Meng − *Department of Chemistry and Shanghai Key Laboratory of Molecular Catalysis and Innovative Materials, Fudan University, Shanghai 200438, P. R. China*

Jinling Wang − *National Engineering Laboratory for Industrial Wastewater Treatment, East China University of Science and Technology, Shanghai 200237, P. R. China;* orcid.org/0000-0002-8654-0803

Chenglin Jia − *Department of Chemistry and Shanghai Key Laboratory of Molecular Catalysis and Innovative Materials, Fudan University, Shanghai 200438, P. R. China*

Tao Liu − *Department of Chemistry and Shanghai Key Laboratory of Molecular Catalysis and Innovative Materials, Fudan University, Shanghai 200438, P. R. China*

Zhi-Pan Liu − *Department of Chemistry and Shanghai Key Laboratory of Molecular Catalysis and Innovative Materials,*

https://dx.doi.org/10.1021/jacs.0c11307
J. Am. Chem. Soc. 2021, 143, 1493−1502

Fudan University, Shanghai 200438, P. R. China; Key Laboratory of Computational Physical Science, Fudan University, Shanghai 200438, P. R. China; orcid.org/0000-0002-2906-5217

Complete contact information is available at: https://pubs.acs.org/10.1021/jacs.0c11307

Notes

The authors declare no competing financial interest.

■ ACKNOWLEDGMENTS

M.G. acknowledges supports from the National Key R&D program of China (2019YFC1604602). X.J.Y. acknowledges supports from the National Key Basic Research Program of China (2019YFC1906700) and National Natural Science Foundation of China (21876049, 51878643). Y.F.L. acknowledges supports from National Natural Science Foundation of China (21972023, 21773032). We thank Prof. Harry Gray, Prof. Emily Carter, Prof. Xile Hu, and Dr. John Martirez for the helpful discussion.

■ REFERENCES

(1) Katsounaros, I.; Cherevko, S.; Zeradjanin, A. R.; Mayrhofer, K. J. Oxygen Electrochemistry as a Cornerstone for Sustainable Energy Conversion. *Angew. Chem., Int. Ed.* **2014**, *53* (1), 102−121.

(2) Gray, H. B. Powering the Planet with Solar Fuel. *Nat. Chem.* **2009**, *1* (1), 7−7.

(3) Carmo, M.; Fritz, D. L.; Mergel, J.; Stolten, D. A Comprehensive Review on PEM Water Electrolysis. *Int. J. Hydrogen Energy* **2013**, *38* (12), 4901−4934.

(4) Zeng, K.; Zhang, D. Recent Progress in Alkaline Water Electrolysis for Hydrogen Production and Applications. *Prog. Energy Combust. Sci.* **2010**, *36* (3), 307−326.

(5) Darcy, J. W.; Koronkiewicz, B.; Parada, G. A.; Mayer, J. M. A Continuum of Proton-Coupled Electron Transfer Reactivity. *Acc. Chem. Res.* **2018**, *51* (10), 2391−2399.

(6) Suen, N. T.; Hung, S. F.; Quan, Q.; Zhang, N.; Xu, Y. J.; Chen, H. M. Electrocatalysis for the Oxygen Evolution Reaction: Recent Development and Future Perspectives. *Chem. Soc. Rev.* **2017**, *46* (2), 337−365.

(7) Li, J.; Güttinger, R.; Moré, R.; Song, F.; Wan, W.; Patzke, G. R. Frontiers of Water Oxidation: the Quest for True Catalysts. *Chem. Soc. Rev.* **2017**, *46* (20), 6124−6147.

(8) Jiao, Y.; Zheng, Y.; Jaroniec, M.; Qiao, S. Z. Design of Electrocatalysts for Oxygen and Hydrogen-Involving Energy Conversion Reactions. *Chem. Soc. Rev.* **2015**, *44* (8), 2060−2086.

(9) Wang, Y.; Yan, D.; El Hankari, S.; Zou, Y.; Wang, S. Recent Progress on Layered Double Hydroxides and Their Derivatives for Electrocatalytic Water Splitting. *Adv. Sci.* **2018**, *5* (8), 1800064.

(10) Lv, L.; Yang, Z.; Chen, K.; Wang, C.; Xiong, Y. 2D Layered Double Hydroxides for Oxygen Evolution Reaction: From Fundamental Design to Application. *Adv. Energy Mater.* **2019**, *9* (17), 1803358.

(11) Gong, M.; Li, Y.; Wang, H.; Liang, Y.; Wu, J. Z.; Zhou, J.; Wang, J.; Regier, T.; Wei, F.; Dai, H. An Advanced Ni-Fe Layered Double Hydroxide Electrocatalyst for Water Oxidation. *J. Am. Chem. Soc.* **2013**, *135* (23), 8452−8455.

(12) Gong, M.; Dai, H. A Mini Review of NiFe-Based Materials as Highly Active Oxygen Evolution Reaction Electrocatalysts. *Nano Res.* **2015**, *8* (1), 23−39.

(13) Dionigi, F.; Strasser, P. NiFe-Based (Oxy)hydroxide Catalysts for Oxygen Evolution Reaction in Non-Acidic Electrolytes. *Adv. Energy Mater.* **2016**, *6* (23), 1600621.

(14) Trzesniewski, B. J.; Diaz-Morales, O.; Vermaas, D. A.; Longo, A.; Bras, W.; Koper, M. T.; Smith, W. A. In Situ Observation of Active Oxygen Species in Fe-Containing Ni-Based Oxygen Evolution Catalysts: The Effect of pH on Electrochemical Activity. *J. Am. Chem. Soc.* **2015**, *137* (48), 15112−15121.

(15) Lee, S.; Banjac, K.; Lingenfelder, M.; Hu, X. Oxygen Isotope Labeling Experiments Reveal Different Reaction Sites for the Oxygen Evolution Reaction on Nickel and Nickel Iron Oxides. *Angew. Chem., Int. Ed.* **2019**, *58* (30), 10295−10299.

(16) Friebel, D.; Louie, M. W.; Bajdich, M.; Sanwald, K. E.; Cai, Y.; Wise, A. M.; Cheng, M.-J.; Sokaras, D.; Weng, T.-C.; Alonso-Mori, R.; Davis, R. C.; Bargar, J. R.; Norskov, J. K.; Nilsson, A.; Bell, A. T. Identification of Highly Active Fe Sites in (Ni,Fe)OOH for Electrocatalytic Water Splitting. *J. Am. Chem. Soc.* **2015**, *137* (3), 1305−1313.

(17) Chen, J. Y. C.; Dang, L.; Liang, H.; Bi, W.; Gerken, J. B.; Jin, S.; Alp, E. E.; Stahl, S. S. Operando Analysis of NiFe and Fe Oxyhydroxide Electrocatalysts for Water Oxidation: Detection of Fe^{4+} by Mössbauer Spectroscopy. *J. Am. Chem. Soc.* **2015**, *137* (48), 15090−15093.

(18) Louie, M. W.; Bell, A. T. An Investigation of Thin-Film Ni-Fe Oxide Catalysts for the Electrochemical Evolution of Oxygen. *J. Am. Chem. Soc.* **2013**, *135* (33), 12329−12337.

(19) Ahn, H. S.; Bard, A. J. Surface Interrogation Scanning Electrochemical Microscopy of $Ni_{(1-x)}Fe_{(x)}OOH$ ($0 < x < 0.27$) Oxygen Evolving Catalyst: Kinetics of the "Fast" Iron Sites. *J. Am. Chem. Soc.* **2016**, *138* (1), 313−318.

(20) Zhang, J.; Liu, J.; Xi, L.; Yu, Y.; Chen, N.; Sun, S.; Wang, W.; Lange, K. M.; Zhang, B. Single-atom Au/NiFe Layered Double Hydroxide Electrocatalyst: Probing the Origin of Activity for Oxygen Evolution Reaction. *J. Am. Chem. Soc.* **2018**, *140* (11), 3876−3879.

(21) Zhu, K.; Zhu, X.; Yang, W. Application of In Situ Techniques for the Characterization of NiFe-based Oxygen Evolution Reaction (OER) Electrocatalysts. *Angew. Chem., Int. Ed.* **2019**, *58* (5), 1252−1265.

(22) Lee, S.; Bai, L.; Hu, X. Deciphering iron-Dependent Activity in Oxygen Evolution Catalyzed by Nickel−iron Layered Double Hydroxide. *Angew. Chem., Int. Ed.* **2020**, *59* (21), 8072−8077.

(23) Sayler, R. I.; Hunter, B. M.; Fu, W.; Gray, H. B.; Britt, R. D. EPR Spectroscopy of Iron- and Nickel-doped [ZnAl]-Layered Double Hydroxides: Modeling Active Sites in Heterogeneous Water Oxidation Catalysts. *J. Am. Chem. Soc.* **2020**, *142* (4), 1838−1845.

(24) González-Flores, D.; Klingan, K.; Chernev, P.; Loos, S.; Mohammadi, M. R.; Pasquini, C.; Kubella, P.; Zaharieva, I.; Smith, R. D. L.; Dau, H. Nickel-iron Catalysts for Electrochemical Water Oxidation − Redox Synergism Investigated by in Situ X-ray Spectroscopy with Millisecond Time Resolution. *Sustainable Energy & Fuels* **2018**, *2* (9), 1986−1994.

(25) Ali-Löytty, H.; Louie, M. W.; Singh, M. R.; Li, L.; Sanchez Casalongue, H. G.; Ogasawara, H.; Crumlin, E. J.; Liu, Z.; Bell, A. T.; Nilsson, A.; Friebel, D. Ambient-Pressure XPS Study of a Ni−Fe Electrocatalyst for the Oxygen Evolution Reaction. *J. Phys. Chem. C* **2016**, *120* (4), 2247−2253.

(26) Li, N.; Bediako, D. K.; Hadt, R. G.; Hayes, D.; Kempa, T. J.; von Cube, F.; Bell, D. C.; Chen, L. X.; Nocera, D. G. Influence of Iron Doping on Tetravalent Nickel Content in Catalytic Oxygen Evolving Films. *Proc. Natl. Acad. Sci. U. S. A.* **2017**, *114* (7), 1486−1491.

(27) Martirez, J. M. P.; Carter, E. A. Unraveling Oxygen Evolution on Iron-doped β-Nickel Oxyhydroxide: The Key Role of Highly Active Molecular-like Sites. *J. Am. Chem. Soc.* **2019**, *141* (1), 693−705.

(28) Martirez, J. M. P.; Carter, E. A. Secondary Transition-Metal Dopants for Enhanced Electrochemical O_2 Formation and Desorption on Fe-Doped β-NiOOH. *ACS Energy. Lett.* **2020**, *5* (3), 962−967.

(29) Xiao, H.; Shin, H.; Goddard, W. A. Synergy Between Fe and Ni in the Optimal Performance of (Ni,Fe)OOH Catalysts for the Oxygen Evolution Reaction. *Proc. Natl. Acad. Sci. U. S. A.* **2018**, *115* (23), 5872−5877.

(30) Shin, H.; Xiao, H.; Goddard, W. A. In Silico Discovery of New Dopants for Fe-Doped Ni Oxyhydroxide ($Ni_{1-x}Fe_xOOH$) Catalysts for Oxygen Evolution Reaction. *J. Am. Chem. Soc.* **2018**, *140* (22), 6745−6748.

(31) Tao, H. B.; Xu, Y.; Huang, X.; Chen, J.; Pei, L.; Zhang, J.; Chen, J. G.; Liu, B. A General Method to Probe Oxygen Evolution Intermediates at Operating Conditions. *Joule.* **2019**, *3* (6), 1498−1509.
(32) Yang, C.; Fontaine, O.; Tarascon, J. M.; Grimaud, A. Chemical Recognition of Active Oxygen Species on the Surface of Oxygen Evolution Reaction Electrocatalysts. *Angew. Chem., Int. Ed.* **2017**, *56* (30), 8652−8656.
(33) Lee, Y. M.; Kim, S.; Ohkubo, K.; Kim, K. H.; Nam, W.; Fukuzumi, S. Unified Mechanism of Oxygen Atom Transfer and Hydrogen Atom Transfer Reactions with a Triflic Acid-Bound Nonheme Manganese(IV)-Oxo Complex via Outer-Sphere Electron Transfer. *J. Am. Chem. Soc.* **2019**, *141* (6), 2614−2622.
(34) Li, J.; Liao, H. J.; Tang, Y.; Huang, J. L.; Cha, L.; Lin, T. S.; Lee, J. L.; Kurnikov, I. V.; Kurnikova, M. G.; Chang, W. C.; Chan, N. L.; Guo, Y. Epoxidation Catalyzed by the Nonheme Iron(II)- and 2-Oxoglutarate-Dependent Oxygenase, AsqJ: Mechanistic Elucidation of Oxygen Atom Transfer by a Ferryl Intermediate. *J. Am. Chem. Soc.* **2020**, *142* (13), 6268−6284.
(35) Holm, R. H. Metal-Centered Oxygen Atom Transfer Reactions. *Chem. Rev.* **1987**, *87* (6), 1401−1449.
(36) Gunay, A.; Theopold, K. H. C-H Bond Activations by Metal Oxo Compounds. *Chem. Rev.* **2010**, *110* (2), 1060−1081.
(37) Zhou, M.; Crabtree, R. H. C−H Oxidation by Platinum Group Metal Oxo or Peroxo Species. *Chem. Soc. Rev.* **2011**, *40* (4), 1875−1884.
(38) Lim, M. H.; Rohde, J.-U.; Stubna, A.; Bukowski, M. R.; Costas, M.; Ho, R. Y. N.; Münck, E.; Nam, W.; Que, L. An Fe-IV = O Complex of a Tetradentate Tripodal Nonheme Ligand. *Proc. Natl. Acad. Sci. U. S. A.* **2003**, *100* (7), 3665−3670.
(39) Wang, H.; Casalongue, H. S.; Liang, Y.; Dai, H. $Ni(OH)_2$ Nanoplates Grown on Graphene as Advanced Electrochemical Pseudocapacitor Materials. *J. Am. Chem. Soc.* **2010**, *132* (21), 7472−7477.
(40) Trotochaud, L.; Young, S. L.; Ranney, J. K.; Boettcher, S. W. Nickel-iron Oxyhydroxide Oxygen-Evolution Electrocatalysts: The Role of Intentional and Incidental Iron Incorporation. *J. Am. Chem. Soc.* **2014**, *136* (18), 6744−6753.
(41) Burstein, G. T. Special issue-A Century of Tafel's Equation: A Commemorative Issue of Corrosion Science. *Corros. Sci.* **2005**, *47* (12), 2855−2856.
(42) Bockris, J. O. Kinetics of Activation Controlled Consecutive Electrochemical Reactions: Anodic Evolution of Oxygen. *J. Chem. Phys.* **1956**, *24* (4), 817−827.
(43) Bediako, D. K.; Surendranath, Y.; Nocera, D. G. Mechanistic Studies of the Oxygen Evolution Reaction Mediated by a Nickel-Borate Thin Film Electrocatalyst. *J. Am. Chem. Soc.* **2013**, *135* (9), 3662−3674.
(44) Yeo, B. S.; Klaus, S. L.; Ross, P. N.; Mathies, R. A.; Bell, A. T. Identification of Hydroperoxy Species as Reaction Intermediates in the Electrochemical Evolution of Oxygen on Gold. *ChemPhysChem* **2010**, *11* (9), 1854−1857.
(45) Li, L.-F.; Li, Y.-F.; Liu, Z.-P. Oxygen Evolution Activity on NiOOH Catalysts: Four-Coordinated Ni Cation as the Active Site and the Hydroperoxide Mechanism. *ACS Catal.* **2020**, *10* (4), 2581−2590.
(46) Li, Y.-F.; Selloni, A. Mechanism and Activity of Water Oxidation on Selected Surfaces of Pure and Fe-Doped NiO_x. *ACS Catal.* **2014**, *4* (4), 1148−1153.
(47) Dionigi, F.; Zeng, Z.; Sinev, I.; Merzdorf, T.; Deshpande, S.; Lopez, M. B.; Kunze, S.; Zegkinoglou, I.; Sarodnik, H.; Fan, D.; Bergmann, A.; Drnec, J.; Araujo, J. F.; Gliech, M.; Teschner, D.; Zhu, J.; Li, W. X.; Greeley, J.; Cuenya, B. R.; Strasser, P. In-situ structure and catalytic mechanism of NiFe and CoFe layered double hydroxides during oxygen evolution. *Nat. Commun.* **2020**, *11* (1), 2522.

https://dx.doi.org/10.1021/jacs.0c11307
J. Am. Chem. Soc. 2021, 143, 1493−1502